Title

Solubility-Dependent Protective Effects of Binary Alloys for Lithium Anode

Journal

ACS Applied Energy Materials, 3(3)

ISSN

2574-0962

Authors

Xu, Yan
Zhao, Shuyang
Zhou, Guangmin
et al.

Publication Date

2020-03-23

DOI

10.1021/acsaem.9b02125

Solubility-dependent protective effects of binary alloys for lithium anode

Yan Xu,[‡] Guangmin Zhou,[⊥] Shuyang Zhao,[♯] Fei Zhou,[Φ] Ze Rong,[Φ] Allen Pei,[⊥] Feifei Shi,[⊥] Wei Chen,[⊥] Hao Chen,[⊥] Yang Wu,[§] Zhenghui Pan,[‡] Jia Li,[♯] Jinghua Guo,*[,‖] Yuegang Zhang*[,‡,§]

‡ i-Lab, Suzhou Institute of Nano-Tech and Nano-Bionics, Chinese Academy of Sciences, Suzhou, Jiangsu, 215123, China

⊥Department of Materials Science and Engineering, Stanford University, Stanford, CA 94305, USA

♯ Laboratory for Computation Materials Engineering, Division of Energy and Environment, Graduate School at Shenzhen, Tsinghua University, Shenzhen 518055, P. R, China;

Φ Monta Vista Energy Technologies Corporation, Hefei, 230601, P. R, China;

‖Advanced Light Source, Lawrence Berkeley National Laboratory, Berkeley, California 94720, United States

§ Department of Physics, Tsinghua University, Beijing, 100084, China

Corresponding authors: J. Guo (E-mail: jguo@lbl.gov); Y. Zhang (E-mail: yuegang.zhang@tsinghua.edu.cn)

Abstract: Recently, alloys have been widely utilized as protection layers for homogenize Li growth. However, the protective mechanisms for different alloys are not clearly understood. Herein, guided by the binary phase diagrams, Mg, Au, Zn, Al, Fe and Cu protective layers have been selected for study of their protective abilities and mechanisms. The selected metals can be classified into three categories according to the nature of their associated alloy protective layers: (1) Metals with high solubility in Li while not forming any intermediate line compounds, e.g. Mg, which is good for fast Li stripping. (2) Metals with limited solid solubility but forming stable line compounds with Li upon the lithiation, e.g.

Au, Zn, and Al, where the formed stable line compounds Li_xAu, Li_xZn, Li_xAl will hamper Li kinetics. (3) Metals with negligible mutual solubility and no line compound formation with Li, e.g. Fe and Cu, which block Li stripping path and therefore result in highest polarization voltage.

Introduction

The ever-increasing demands of consumer electronics and grid-scale storage have driven the development of advanced battery systems with high energy density and long cycling life.[1, 2] Rechargeable lithium metal-based batteries (LMBs) have been considered as one of the most promising energy storage devices due to the lowest electrode potential (−3.040 V *vs.* standard hydrogen electrode) and highest theoretical specific capacity (3,860 mAh/g) of Li metal anode.[3, 4] Li metal anode has been paired with conversion based cathodes such as sulfur or oxygen to achieve high energy density batteries.[5, 6, 7, 8] However, dendrite growth and the parasitic reactions between the highly reactive lithium metal and the organic liquid electrolyte are critical obstacles for commercialization of safe and reliable LMBs.[9, 10, 11, 12, 13] Tremendous efforts have been taken to circumvent the safety challenges of Li anodes.[14, 15, 16, 17, 18, 19, 20] For example, solid state electrolytes,[21, 22, 23, 24] engineered solid-electrolyte interphases (SEIs)[25, 26] and smart separators[27] were adopted to suppress dendrite growth. However, the intrinsic dendritic plating of Li has not yet been fully resolved. Recently, alloy strategies have been utilized to homogenize the growth of Li without dendrites. For example, Au nano-seeds have been embedded inside carbon nano-shells to eliminate dendrite growth by Li_xAu formation.[28] Li_xSi alloy has also been designed to avoid the intrinsic problems of volume expansion and dendrite growth.[10] Other Li-based alloys, such as Li_xSn,[29] Li_xZn,[30] and Li_xAs,[31] have been investigated and their protective effects were demonstrated. It is well-known that these effectively protective layers on Li metal are

dense, chemically stable, and with good electronic/ionic conductivity.[32, 33, 34, 35] However, different protective effects and the corresponding mechanisms for different alloy protective layers are not clearly understood so far.

Herein, guided by the binary phase diagrams, a series of metals and their alloys have been selected for a systematic study of their Li anode protective abilities. We find that, due to the high solubility of Mg with Li and the lack of rate-limiting phase transition of Li-metal line compound formation in Li-Mg solid solution, the kinetics of Li insertion and extraction in/from Li-Mg solid solution is fast, which reduces the necessary electrochemical driving force (*i.e.* overpotential) and results in homogeneous Li plating. Therefore, a Li electrode with Mg-based protective layer improves its cycling life, stability, and rate capability. In contrast, Au, Zn, and Al have limited solubility in Li and can form stable line compound alloy phases of Li_xAu, Li_xZn, and Li_xAl upon cycling, which results in sluggish electrochemical kinetics of Li in such alloys. The third category of metals, such as Fe and Cu, display the poorest performance for Li anode protection, due to their insolubility with Li. These results could guide the design of better protective layer for future high energy density LMBs.

Results and discussion

Selection of metal protective layers according to binary phase diagrams.

Binary phase diagrams were used to identify a series of Li-metal alloys for Li protective layers. Au, Zn, and Al were selected as a category of metals that has a low solubility with Li (<1% at room temperature) but can form stable line compound phases upon reaction with Li.[28] On the other hand, Fe and Cu were chosen as a category of metals that have either a negligible solubility with Li (*e.g.* Fe)[36] or a kinetically slow reaction with Li (*e.g.* Cu).[37] In contrast, Mg was identified as a metal with a very high

mutual solubility with Li.[38] Mg does not form any intermediate line compounds along all the binary compositions in Mg-Li binary phase diagram.[38] Instead, Mg and Li can form a solid solution with 0 to ~68 at.% Mg in Li, and another solid solution of 0 to ~15 at.% Li in Mg. This feature allows part of surficial Mg atoms to dissolve into Li, which makes Mg film adheres firmly on Li metal surface.

Fabrication and characterization of metal protective layers. Mg, Au, Zn, Al, Fe and Cu protective layers have been fabricated according to solution-based reaction methods with Li metal. The morphology and thickness of the protective layers are characterized by scanning electron microscopy (SEM). Figure 1 shows a comparison of Mg, Zn and Fe protective layers with pristine Li metal surface without any protection layer. As shown in Figure 1b, the top-view SEM image reveals that Mg protective layer is smooth and uniform, which is helpful for uniform deposition of Li-ions. Figure 1c shows the continuous and compact feature of Zn protective layer. The Fe protective layer also exhibit a uniform morphology (Figure 1d).

In order to evaluate how the solubility affects the adhesion of different protective layers with underneath Li foil, we do a vertical cutting by blade from protective layer side. After cutting by a blade, Mg protective layer still shows a good adhesion with Li foil without the sign of peeling off from Li foil (Figure 1f). For comparison, cracks are shown in the Zn and Fe protective layers (Figure 1g-h) after cutting, and Zn, Fe protective layers are almost detached with Li foil, which indicates Zn and Fe protective layers have poor physical strength and weak adhesion with Li foil. The cutting test indicates Mg protective layer has the best adhesion with Li metal, which can be attribute to the high solubility of Mg in Li.

As shown in Figure S1, the thickness of Mg, Zn and Fe protective layers was measured by cross-

sectional SEM with a thickness of ~8 μm, ~8 μm and ~2 μm, respectively, much larger than ~200 nm calculated from the amount of applied reactants, which may cause by the diffusion of metals in Li and the volume expanded alloys. The compositions of the protective layers were characterized by X-ray diffraction (XRD). Metallic Mg is the only crystalline phase detected in Mg protective layer (Figure 1j), which is consistent with the binary phase diagram. LiZn alloy and metallic Zn are the main phases identified in the Zn protective layer (Figure 1k). The presence of metallic Zn indicates that self-alloying process of Zn with Li is a kinetically limited process. In the Fe protective layer, metallic Fe is the main crystalline composition (Figure 1l). X-ray photoelectron spectroscopy (XPS) further double confirmed the compositions of different protective layers (Figure S2).

Computation of binding energy of Li-Li, Li-Zn and Li-Mg and kinetic characterization of Li-ion in different metal protective layers. The binding energy of Li-Li, Li-Zn and Li-Mg was calculated to confirm the difficulty order of Li removal from Li foil, Zn and Mg protective layers. As shown in Figure 2a, the binding energy of Li-Li, Li-Zn and Li-Mg was calculated to be -1.60 eV, -0.45 eV and -0.13 eV, respectively. The lower the binding energy, the more stable of the structure. The binding energy calculation illustrated that the structural stability order is Li-Li□Li-Zn□Li-Mg, which indicated Li removal kinetics from Mg protective layer is fastest. Further, to compare the kinetics of Li losing electron on different protective layers, charge transfer resistances (R_{ct}) of the protected Li electrodes were evaluated *via* electrochemical impedance spectroscopy (EIS) in symmetric cells (Li with protective layer ‖electrolyte‖ Li with protective layer). The high-frequency semicircles are good indicators of the R_{ct} at the electrode-electrolyte interface. According to the equation of $R_{ct}=RT/nFi_0$ (R is Moore constant, T is Fahrenheit temperature, n is transfer electron number and i_0 is the exchange

current density), we know that if R_{ct} is smaller, i_0 will be greater, and more electron will be transferred. As shown in Figure 2b, because of the unavoidable formation of solid electrolyte interface (SEI) between fresh Li metal and carbonate electrolyte, the blank cell shows an extremely high initial interfacial resistance of ~443 ohms. Remarkably, the symmetric cell with Mg protective layer shows the lowest charge transfer resistances (~77 ohms), which reflects that in the Mg protective layer Li atom owns the highest capacity of losing electron. For the symmetric cells with Zn and Fe protective layers, a much high resistance of ~145 and ~181 ohms could be observed (Figure 2b), which indicates Li atom lose electron is a difficult process in Zn and Fe protective layers, especially in Fe protective layer. These results indicate that Li is hard to strip from Zn, Fe protective layer than Mg protective layer. EIS of the symmetric cells was also measured after 10 cycles at a current density of 1 mA/cm^2 (Figure 2c). For the blank symmetric cell, the charge transfer resistance rapidly decreased to ~85 ohms mainly because of the broken SEI layer as well as largely increased surface area caused by dendrite growth. Meanwhile, the impedances of symmetric cells with Zn, Fe and Mg protective layers decreased to 39 ohms, 44 ohms and 21 ohms, respectively. These results further demonstrate that Li-ion transportation in the Mg protective layer is the fastest among Mg, Zn and Fe protective layers at both the initial and the cycled states.

Electrochemical characterization of the protective effect of different protective layers. To further validate the function of the different protective layers, long-term Li stripping/plating performance measurements were carried out in two-electrode symmetric cells. A practical capacity of Li stripping/plating (2 $mAh \cdot cm^{-2}$) was employed in each discharge/charge cycle for all samples. Figure 3a1-g1 show the voltage profiles as a function of time for Li electrodes with different protective layers.

The polarization voltage of the symmetric cell without protective layer increases gradually after 25 cycles and the corresponding SEM images after 5 cycles show that Li foil surface is covered with numerous entangled dendrites (Figure 3a2, a3). In contrast, the symmetric cell with Mg protective layer shows the best performance that maintains stable cycling over 100 cycles and the overpotential as low as 0.07 V (Figure 3b1), which confirm the fast kinetics of Li stripping with Mg protective layer. The corresponding SEM image of the Mg protective layer after 5 cycles shows a smooth and uniform Li deposition morphology without Li protrusions (Figure 3b2). In the magnified SEM image (Figure 3b3), densely packed nodule-like Li crystals can be seen on the Mg protective layer. For the cases with Au, Zn, and Al protective layers, the cells' cycling performances were improved compared to that of the blank cell but weren't as good as Mg case. As shown in Figure 3c1, d1 and e1, the cycling life of symmetric cells with Au, Al and Zn protective layers can reach 90 cycles, 40 cycles and 50 cycles, respectively. The polarization voltages with Au, Al and Zn protective layers were 0.105 V, 0.118 V and 0.094 V in the first decades cycles and gradually increase with time. The higher polarization voltage with Au, Al and Zn protective layers suggested alloy protective layers hamper lithium kinetics. The SEM observation reveals that tiny dendrites growth can be seen on the Au, Al and Zn protective layers after cycling (Figure 3c2, c3, d2, d3, e2 and e3). As for Fe and Cu cases, the cycle lives with Fe and Cu protective layers were 60 cycles (Figure 3f1) and 25 cycles (Figure 3g1), respectively, and the polarization voltages of first cycle are as high as 0.35 V and 0.94 V, which show the highest polarization voltage among Mg, Au, Al, Zn, Fe, Cu cases. The SEM images in Figure 3f2, f3, g2 and g3 evidence that cracks and dendrites are also generated on cycled Fe and Cu protective layers due to the negligible solubility with Li or a kinetically slow reaction with Li.

To clarify the composition change of the protective layers after Li stripping, XPS and XRD were utilized to characterize the retrieved Li electrodes of stripping states after 5 cycles at a current density of 1 mA/cm^2. For the Li electrode with Mg protective layer, metallic Mg and Li be detected by XRD after cycling (Figure 4a). Also, metallic Mg (50.6 eV) and Li (56 eV) can be detected by XPS. XPS is surface sensitive tool, and the coexistence of Li and Mg in the surface confirm the high diffusivity of Li in Mg, which result in low polarization voltage. While in the Zn protective layer, LiZn alloy is the only Zn containing phase that can be detected by XRD (Figure 4b). Combined with above computation and electrochemical results, a reasonable inference can be made that the stripped Li should be from LiZn alloy and underneath Li will compensate Li loss in LiZn alloy protective layer. LiZn alloy is more stable than Li-Mg solution and more energy is need to remove Li from LiZn alloy, which results in a slow electrochemical kinetics and high polarization voltage in LiZn alloy case. In Zn 2p XPS spectra (Figure 4e), $ZnCO_3$, ZnO and LiZn peaks are observed at 1022.8 eV, 1022.3 eV and 1021.7 eV, which indicates Zn protective layer is not as robust as Mg protective layer to resist the attack of electrolyte. As to the Fe protective layer, Fe signal is absent in both XRD (Figure 4c) and XPS (Figure 4f) test after cycling, which can be attributed to the thick lithium dendrite growth on the surface of Fe protective layer.

In order to demonstrate the effect of these protective layers, full cells were constructed using a $LiCoO_2$ (LCO) cathode paired a bare Li metal anode or Li anodes with Mg, Zn and Fe protective layers. As shown in Figure S5, higher capacity was consistently retained with Mg protective layer, especially at

higher rates, which indicate the fast Li stripping kinetics with Mg protective layer. The LCO/bare Li cell only offers capacities of 135 $mAh \cdot g^{-1}$ at 0.4 C, 128 $mAh \cdot g^{-1}$ at 1 C, 120 $mAh \cdot g^{-1}$ at 2 C, 110 $mAh \cdot g^{-1}$ at 4 C and 80 $mAh \cdot g^{-1}$ at 8 C. In comparison, the LCO/Li cell with Mg protective layer shows 150 $mAh \cdot g^{-1}$ at 0.4 C, 146 $mAh \cdot g^{-1}$ at 1 C, 141 $mAh \cdot g^{-1}$ at 2 C, 131 $mAh \cdot g^{-1}$ at 4 C and 114 $mAh \cdot g^{-1}$ at 8 C. After resetting the rate back to 1 C, the LCO/Li with Mg protective layer can maintain its initial capacity. Although LCO/Li cells with Zn and Fe protective layers show comparable rate performances as LCO/bare Li at low rates, the capacities decay quickly at high rates, confirming the sluggish Li-ion kinetics in Zn and Fe based protective layers under high current densities. It should be noted that the capacity of the LCO/Li cell with Mg protective layer shows much better retention compared to those of with Zn, Fe protective layers and the blank cell (Figure S5b). The significant capacity decay after long cycling in the blank cell and LCO/Li cell with Zn and Fe protective layers may be ascribed to the constant consumption of electrolytes caused by the growth of Li dendrites.

Based on the discussion above, the protective mechanisms of three categories of selected metals during Li plating/ stripping process can be summarized in Figure 5. In the stripping process, Li will strip smoothly from Li-Mg solid solution because of the low Li removal energy from Li-Mg solid solution, which is of importance for fast Li removal kinetics. While in the Au, Zn and Al protective layers cases, take Li_xZn as example, Li will strip from stable line compounds Li_xZn during the stripping process because of the lower binding energy of Li-Zn than Li-Li, and underneath Li will compensate Li loss of stable line compounds Li_xAu, Li_xZn, Li_xAl. Due to the high stability of line compounds Li_xAu, Li_xZn, Li_xAl, more energy is needed to remove Li from Li_xAu, Li_xZn, Li_xAl protective layers than in Li-Mg

solid solution situation, which result in high polarization voltage of this category protective layer. For Fe and Cu protective layers, due to either a negligible solubility with Li (*e.g.* Fe) or a kinetically slow reaction with Li (*e.g.* Cu), this category protective layer will block Li stripping path and result in high polarization voltage. For the plating process, Li will plate smoothly in the Mg protective layer case due to the high solubility of Li in Mg. For the Au, Zn, Al, Fe and Cu cases, Li will plate uniformly on these protective layers at early Li deposition stage due to the limited solubility of Li in these metals, while with the deposited Li increasing, these protective layers will be over-lithiated and tiny dendrites will protrude gradually. For Fe and Cu protective layers, Li will plate directly on the surface and form dendrites due to the negligible mutual solubility of Li with Fe or Cu.

Conclusion

In summary, three categories of metals and associated alloys have been systematically investigated to identify their protective effect on Li metal anode. The experimental results show that the Mg protective layer exhibits much better cycling life, and lower voltage polarization than that of Au, Al, Zn, Fe, and Cu protective layers. It demonstrates that the metal with a high solubility in Li and lack of rate-limiting line compounds will facilitate homogenous Li plating and contribute to better battery performance. The excellent stability of the Mg protective layer is confirmed by the significantly improved performance of LCO/Li full cells. The finding could provide guidance for future design of solid interfaces toward high performance and safe Li metal batteries.

Experimental methods

Preparation of the protected lithium electrode. Electrode preparation was carried out in an argon-filled glove box (O_2 level <10 ppm and H_2O level < 0.5 ppm). Lithium metal foil (99.9%, Aldrich) was

polished to get a shiny surface. After polishing, 50 μL carbonate-based electrolyte (1M $LiPF_6$ in 1:1 EC/DEC, BASF) with 50 mM different additives was dropped onto the lithium foil.

Electrochemical testing. To investigate the electrochemical performances of protected and unprotected Li metal, symmetric type-2032 coin cells were assembled with two identical electrodes. The impedance spectra were recorded over the frequency from 100 kHz to 100 mHz using a Bio-Logic VMP3 system. For the fabrication of LCO cathode, a LCO slurry containing LCO: Super P: PVDF =70:20:10 was coated onto an Al foil with a total mass loading of ~3 mg/cm^2 and dried at 80 ^{o}C under vacuum for 2 days. Coin cells were assembled using a Li metal foil as counter/reference electrode. Galvanostatic cycling of symmetric Li metal cells and Li-LCO cells were carried out on a LAND battery testing system with the potential range of 3.0-4.2 V (*vs.* Li/Li$^+$).

Characterizations. The pristine and cycled Li metal electrodes were mounted onto SEM stages and sealed in Ar-filled transfer vessels for immediate SEM (FEI Quanta 200) observation. Powder X-ray diffraction was performed on a PANalytical X'Pert with Ni-filtered Cu Kα radiation. The XRD samples were sealed with Kapton tape (DuPont). XPS analysis was performed on PHI Versa Probe 5000, Physical Electronics, USA. For sputter depth profiling, Ar^+ ions of 2 keV energy at a scan size of 1 mm×1 mm was utilized.

ACKNOWLEGEMENTS

This work was supported by the National Key Research and Development Program of China (2016YFB0100100), the National Natural Science Foundation of China (No. 21433013), the CAS-DOE Joint Research Program (121E32KYSB20150004), CAS-Queensland Collaborative Science Fund (121E32KYSB20160032). This research used resources of the Advanced Light Source, which is a DOE

Office of Science User Facility under contract no. DE-AC02-05CH11231.

References

1. Chu S, Majumdar A. Opportunities and challenges for a sustainable energy future. *Nature* **488**, 294 (2012).
2. Chu S, Cui Y, Liu N. The path towards sustainable energy. *Nature Materials* **16**, 16 (2016).
3. Goodenough JB, Kim Y. Challenges for Rechargeable Li Batteries. *Chemistry of Materials* **22**, 587-603 (2010).
4. Bruce PG. Energy storage beyond the horizon: Rechargeable lithium batteries. *Solid State Ionics* **179**, 752-760 (2008).
5. Bruce PG, Freunberger SA, Hardwick LJ, Tarascon J-M. Li–O_2 and Li–S batteries with high energy storage. *Nature Materials* **11**, 19 (2011).
6. Yang Y, Zheng G, Cui Y. Nanostructured sulfur cathodes. *Chemical Society Reviews* **42**, 3018-3032 (2013).
7. Qiu Y*, et al.* High-Rate, Ultralong Cycle-Life Lithium/Sulfur Batteries Enabled by Nitrogen-Doped Graphene. *Nano Letters* **14**, 4821-4827 (2014).
8. Zhou G*, et al.* Catalytic oxidation of Li_2S on the surface of metal sulfides for Li–S batteries. *Proceedings of the National Academy of Sciences* **114**, 840-845 (2017).
9. Wang H, Lin D, Liu Y, Li Y, Cui Y. Ultrahigh–current density anodes with interconnected Li metal reservoir through overlithiation of mesoporous AlF_3 framework. *Science Advances* **3**, (2017).
10. Zhao J*, et al.* Air-stable and freestanding lithium alloy/graphene foil as an alternative to lithium metal anodes. *Nature Nanotechnology* **12**, 993 (2017).
11. Tarascon JM, Armand M. Issues and challenges facing rechargeable lithium batteries. *Nature* **414**, 359 (2001).
12. Shi F*, et al.* Lithium metal stripping beneath the solid electrolyte interphase. *Proceedings of the National Academy of Sciences* **115**, 8529-8534 (2018).
13. Shi F*, et al.* Strong texturing of lithium metal in batteries. *Proceedings of the National Academy of Sciences* **114**, 12138-12143 (2017).
14. Lin D*, et al.* Layered reduced graphene oxide with nanoscale interlayer gaps as a stable host for lithium metal anodes. *Nature Nanotechnology* **11**, 626 (2016).
15. Li W*, et al.* The synergetic effect of lithium polysulfide and lithium nitrate to prevent lithium dendrite growth. *Nature Communications* **6**, 7436 (2015).
16. Lu Y, Tu Z, Archer LA. Stable lithium electrodeposition in liquid and nanoporous solid electrolytes. *Nature Materials* **13**, 961 (2014).
17. Tu Z, Nath P, Lu Y, Tikekar MD, Archer LA. Nanostructured Electrolytes for Stable Lithium Electrodeposition in Secondary Batteries. *Accounts of Chemical Research* **48**, 2947-2956 (2015).
18. Suo L, Hu Y-S, Li H, Armand M, Chen L. A new class of Solvent-in-Salt electrolyte for high-energy rechargeable metallic lithium batteries. *Nature Communications* **4**, 1481 (2013).
19. Liu K*, et al.* Lithium Metal Anodes with an Adaptive "Solid-Liquid" Interfacial Protective Layer.

Journal of the American Chemical Society **139**, 4815-4820 (2017).
20. Wang H*, et al.* A reversible dendrite-free high-areal-capacity lithium metal electrode. *Nature Communications* **8**, 15106 (2017).
21. Kamaya N*, et al.* A lithium superionic conductor. *Nature Materials* **10**, 682 (2011).
22. Thangadurai V, Narayanan S, Pinzaru D. Garnet-type solid-state fast Li ion conductors for Li batteries: critical review. *Chemical Society Reviews* **43**, 4714-4727 (2014).
23. Wang C*, et al.* Suppression of Lithium Dendrite Formation by Using LAGP-PEO (LiTFSI) Composite Solid Electrolyte and Lithium Metal Anode Modified by PEO (LiTFSI) in All-Solid-State Lithium Batteries. *ACS Applied Materials & Interfaces* **9**, 13694-13702 (2017).
24. Liu Y*, et al.* Transforming from planar to three-dimensional lithium with flowable interphase for solid lithium metal batteries. *Science Advances* **3**, (2017).
25. Yan K*, et al.* Ultrathin Two-Dimensional Atomic Crystals as Stable Interfacial Layer for Improvement of Lithium Metal Anode. *Nano Letters* **14**, 6016-6022 (2014).
26. Kozen AC*, et al.* Next-Generation Lithium Metal Anode Engineering via Atomic Layer Deposition. *ACS Nano* **9**, 5884-5892 (2015).
27. Lin D, Zhuo D, Liu Y, Cui Y. All-Integrated Bifunctional Separator for Li Dendrite Detection via Novel Solution Synthesis of a Thermostable Polyimide Separator. *Journal of the American Chemical Society* **138**, 11044-11050 (2016).
28. Yan K*, et al.* Selective deposition and stable encapsulation of lithium through heterogeneous seeded growth. *Nature Energy* **1**, 16010 (2016).
29. Tu Z*, et al.* Fast ion transport at solid–solid interfaces in hybrid battery anodes. *Nature Energy*, (2018).
30. Wang C*, et al.* Conformal, Nanoscale ZnO Surface Modification of Garnet-Based Solid-State Electrolyte for Lithium Metal Anodes. *Nano Letters* **17**, 565-571 (2017).
31. Liang X*, et al.* A facile surface chemistry route to a stabilized lithium metal anode. *Nature Energy* **2**, 17119 (2017).
32. Marchioni F*, et al.* Protection of Lithium Metal Surfaces Using Chlorosilanes. *Langmuir* **23**, 11597-11602 (2007).
33. Umeda GA, Menke E, Richard M, Stamm KL, Wudl F, Dunn B. Protection of lithium metal surfaces using tetraethoxysilane. *Journal of Materials Chemistry* **21**, 1593-1599 (2011).
34. Li Y*, et al.* Robust Pinhole-free Li3N Solid Electrolyte Grown from Molten Lithium. *ACS Central Science* **4**, 97-104 (2018).
35. Basile A, Bhatt AI, O'Mullane AP. Stabilizing lithium metal using ionic liquids for long-lived batteries. *Nature Communications* **7**, ncomms11794 (2016).
36. Predel B. Fe-Li (Iron-Lithium). In: *Dy-Er–Fr-Mo*. Springer Berlin Heidelberg (1995).
37. Rehnlund D*, et al.* Lithium trapping in alloy forming electrodes and current collectors for lithium based batteries. *Energy & Environmental Science* **10**, 1350-1357 (2017).
38. Shi Z, Liu M, Naik D, Gole JL. Electrochemical properties of Li–Mg alloy electrodes for lithium batteries. *Journal of Power Sources* **92**, 70-80 (2001).
39. Dedryvère R, Gireaud L, Grugeon S, Laruelle S, Tarascon JM, Gonbeau D. Characterization of Lithium Alkyl Carbonates by X-ray Photoelectron Spectroscopy: Experimental and Theoretical Study. *The Journal of Physical Chemistry B* **109**, 15868-15875 (2005).

40. Aurbach D, Gamolsky K, Markovsky B, Gofer Y, Schmidt M, Heider U. On the use of vinylene carbonate (VC) as an additive to electrolyte solutions for Li-ion batteries. *Electrochimica Acta* **47**, 1423-1439 (2002).

Author Contribution

Y. X., G. Z, J. G., Y. C. and Y. Z conceived the concept, Y. X. carry out electrochemical experiments, Y. X., G. Z., W. C., F. S. and H. C. conducted SEM, XRD, XPS. Y. X., G. Z, J. G., Y. C. and Y. Z co-wrote the paper. All authors discussed the results and commented on the manuscript.

Competing financial interests

The authors declare no competing financial interests.

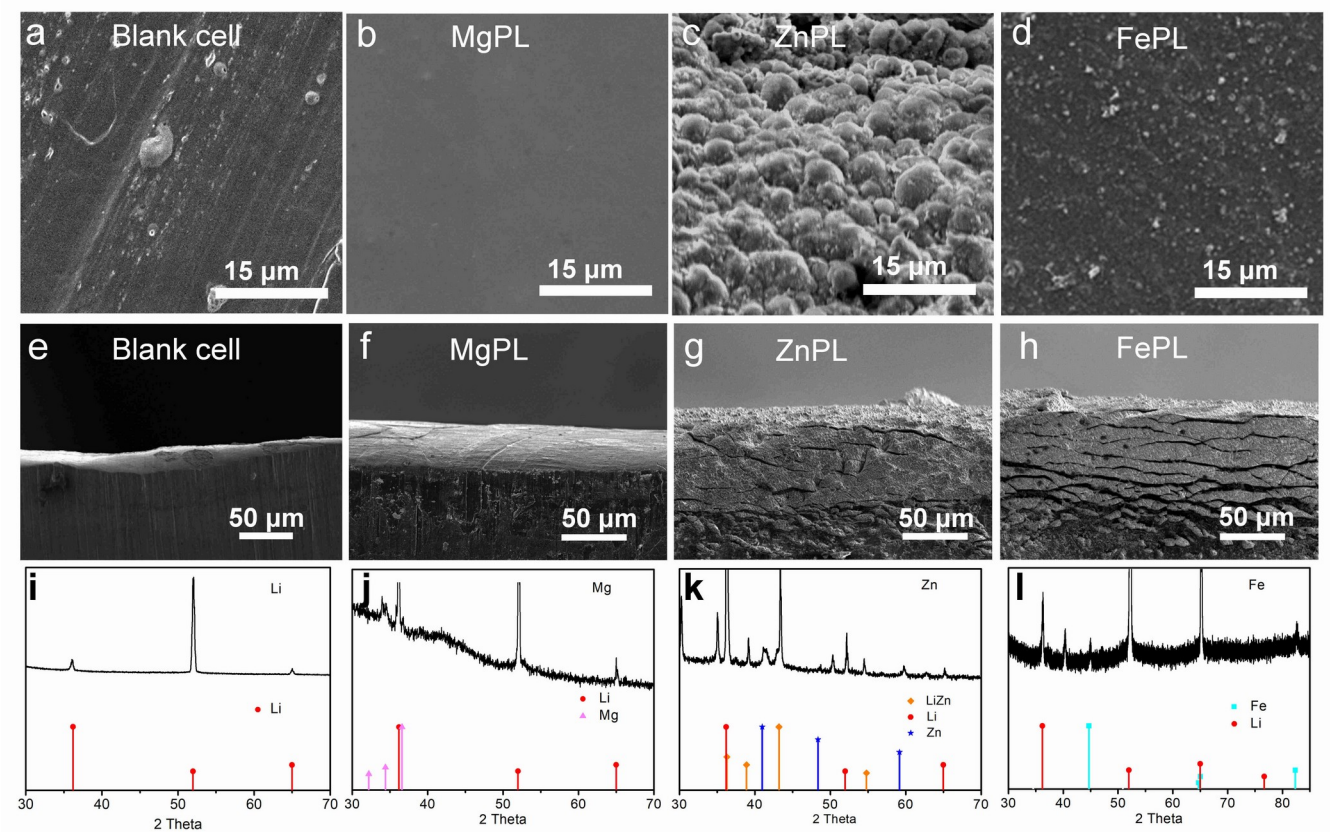

Figure 1 | Characterization of different protective layers. SEM images of the metallic Li surface (a) without protective layer, (b) with Mg protective layer (MgPL), (c) with Zn protective layer (ZnPL), and (d) with Fe protective layer (FePL). Cross-sectional SEM images of lithium surface after bending of (e) without protective layer, (f) with MgPL, (g) with ZnPL and (h) with FePL. XRD characterizations of Li surface (i) without protective layer, (g) with MgPL, (k) with ZnPL, and (l) with FePL, respectively.

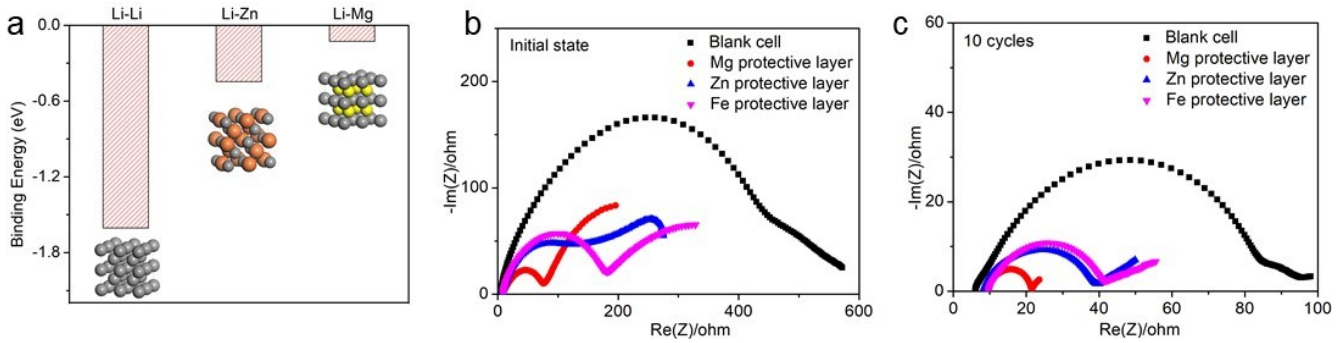

Figure 2 | Computation of binding energy of Li-Li, Li-Zn and Li-Mg and kinetic characterization of Li-ion in different metal protective layers. (a) The binding energy of Li-Li, Li-Zn and Li-Mg was calculated by density functional theory (DFT). Nyquist plots of the impedance spectra of the symmetric Li cells without protective layer (black), with Mg protective layer (red), Zn protective layer (blue) and Fe protective layer (purple) (a) at initial state and (b) after 10 cycles at a current density of 1 mA/cm^2.

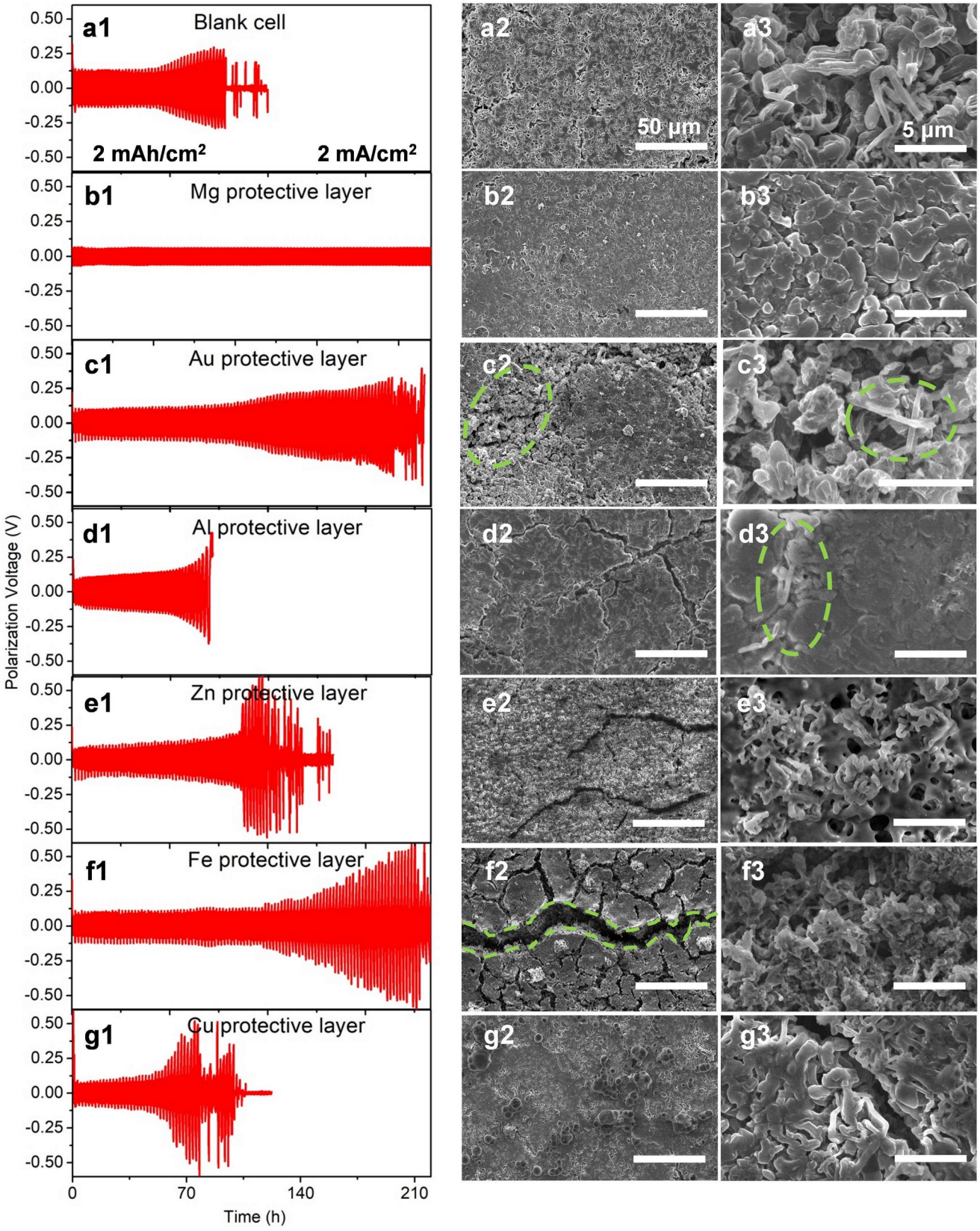
a1
Blank cell
2 mAh/cm²
2 mA/cm²
b1
Mg protective layer
c1
Au protective layer
d1
Al protective layer
e1
Zn protective layer
f1
Fe protective layer
g1
Cu protective layer
Polarization Voltage (V)
0.50
0.25
0.00
-0.25
-0.50
0
70
140
210
Time (h)
a2
50 μm
a3
5 μm
b2
b3
c2
c3
d2
d3
e2
e3
f2
f3
g2
g3

Figure 3 | Electrochemical performance of different protective layers and corresponding morphological evolution. (a1-g1) The voltage profiles with different protective layers as a function of time at the current density of 2 mA/cm^2, and (a2-g2, a3-g3) the corresponding SEM images of lithium metal retrieved from electrolyte after 5 cycles. Scale bar: 50 μm and 5 μm.

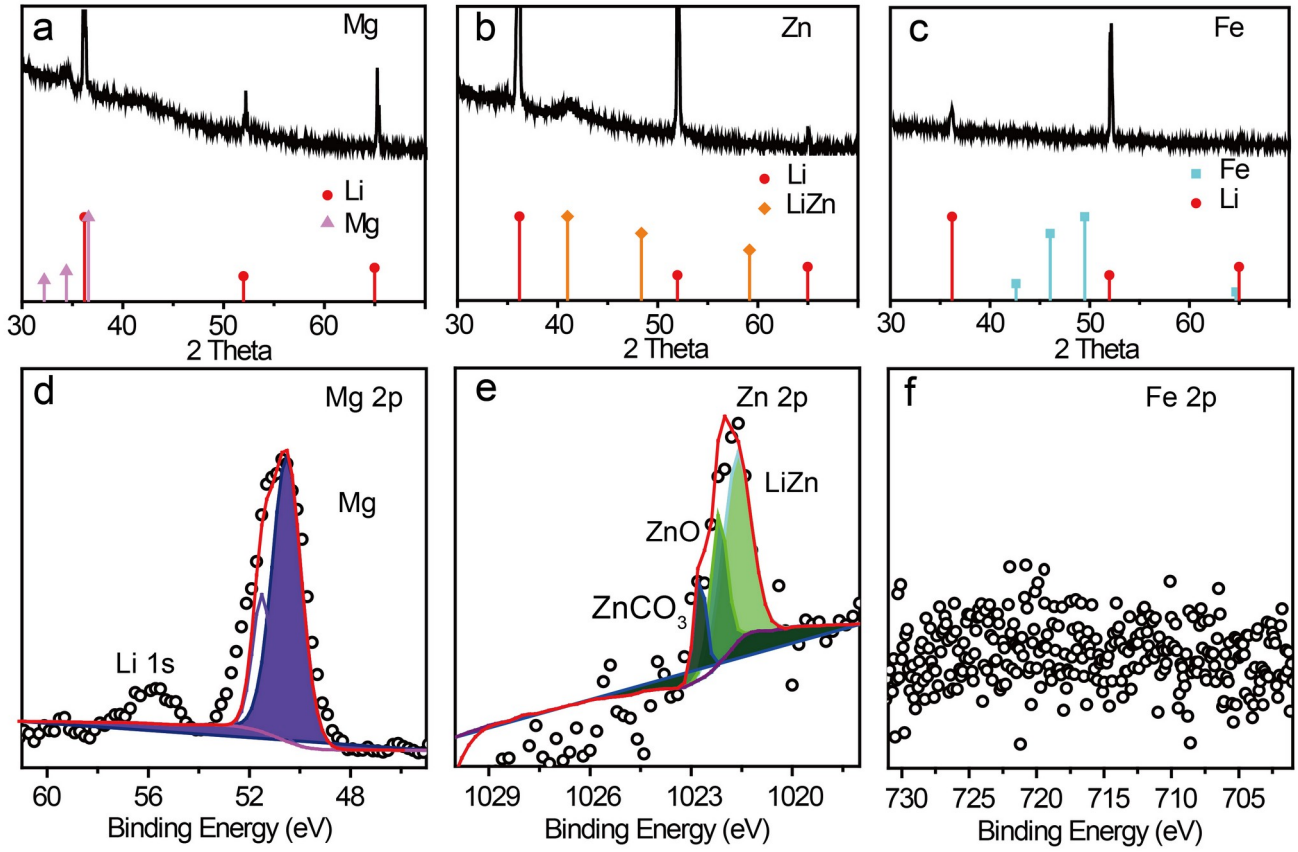

Figure 4 | Characterization of the components of protective layers on cycled Li anode. XRD characterization for the composition of (a) Mg, (b) Zn and (c) Fe protective layers after 5 cycles in symmetric cells at a current density of 1 mA/cm^2.

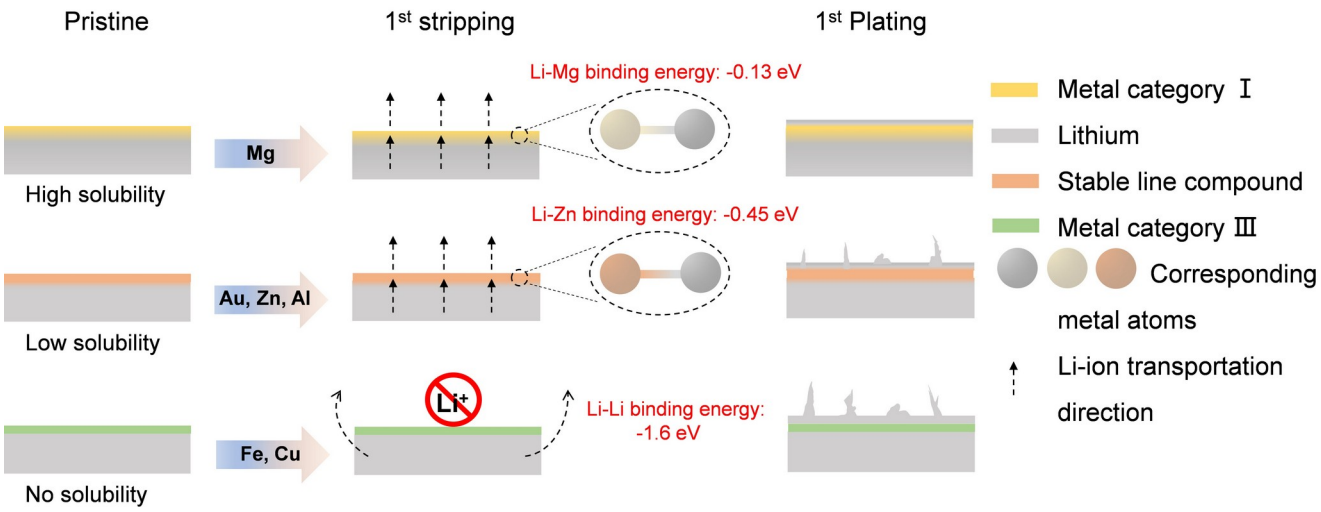

Figure 5 | Schematic diagram showing the Li plating with different protective layers.